PHYSICAL REVIEW B VOLUME 20, NUMBER 2 15 JULY 1979

Extended-x-ray-absorption-fine-structure studies of low-Z atoms in solids and on surfaces: Studies of Si_3N_4, SiO_2, and oxygen on Si(111)

J. Stöhr, L. Johansson, I. Lindau, and P. Pianetta*

Stanford Synchrotron Radiation Laboratory, Stanford University, Stanford, California 94305

(Received 30 November 1978)

Extended-x-ray-abosorption-fine-structure (EXAFS) studies above the nitrogen (~ 400 eV) and oxygen (~ 535 eV) K absorption edges are reported for silicon nitride, silicon dioxide, and oxygen on a Si (111) surface. Measurements were carried out using soft-x-ray synchrotron radiation and employing the surface-sensitive secondary-electron-yield detection technique. EXAFS spectra of bulk Si_3N_4 and SiO_2 are analyzed to test the reliability of theoretical phase shifts and to derive experimental ones for the N-Si and O-Si systems. It is found that nearest-neighbor distances from low-Z atoms can be determined to an accuracy of $\lesssim$ 0.03 Å and second-nearest-neighbor separations to $\lesssim$ 0.05 Å using calculated phase shifts. The surface EXAFS spectrum of one of the initial oxidation stages (characterized by a Si $2p$ chemical shift of 2.5 eV) reveals that the O–Si bond length is slightly (0.04 Å) larger than in SiO_2. Analysis of the relative EXAFS amplitudes provides information on the oxygen-bonding geometry on the Si (111) surface. The importance and advantage of polarization-dependent surface EXAFS studies are discussed.

I. INTRODUCTION

Extended-x-ray-absorption-fine-structure (EXAFS)[1] studies above low-Z K edges, especially carbon (~285 eV), nitrogen (~400 eV), and oxygen (~535 eV), appear to have a great number of applications in a variety of research fields. They could shed light on structural problems in *polymer* research which has recently become the focus of interest in the photographic and electronic industries.[2] Many commercially important amorphous materials, especially *glasses*,[3] contain oxygen, and EXAFS might help to clarify the question about nearest-neighbor coordination numbers in such systems. Finally, low-Z atoms and molecules play a dominant role in *surface science*, a field which has recently received attention partly because of its direct implications for the understanding of heterogeneous *catalysis*. It is clear that the study of carbon, nitrogen, and oxygen containing molecules on surfaces by means of EXAFS could provide valuable information on the structure of surface complexes which are present or formed in catalytic reactions.[4] The *oxidation* of surfaces is one of the most intensely studied phenomena in surface science.[5] In many instances, however, especially when oxidation does not involve the formation of an ordered oxygen overlayer on the surface, little is known about the structure of the oxygen-substrate complexes formed during the initial steps of oxidation. Again, EXAFS data, if obtainable, could give detailed structural information.

In the past, EXAFS studies of low-Z atoms have been hindered mainly by the unavailability of monochromatic x rays in the spectral range between the carbon K edge (~285 eV) and a few keV.[6] Even with the availability of high-flux synchrotron radiation, problems still exist in the aforementioned photon energy range. This is illustrated in Fig. 1 which shows the photon flux in the range $50 \leq h\nu \leq 1000$ eV measured as the photoyield of a Au target-

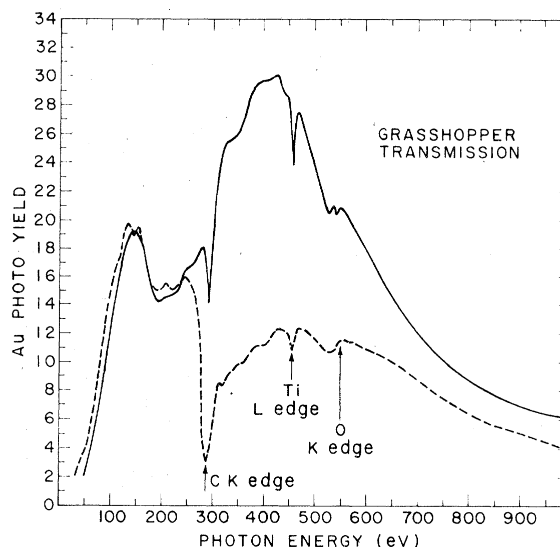

FIG. 1. Transmission function of the grasshopper monochromator at SSRL measured as the photo yield from a Au sample. The solid line was recorded immediately after new optical elements were installed, and the dashed curve was obtained (Ref. 9) four months later illustrating the carbon contamination buildup. The two curves have been normalized with respect to each other by assuming that the photon flux at $h\nu = 150$ eV remains unchanged.

 © 1979 The American Physical Society

get emerging from the grazing incidence monochromator grasshopper[7] at the Stanford Synchrotron Radiation Laboratory (SSRL) on the storage ring SPEAR. The photon flux emitted by SPEAR over the energy range shown is nearly constant such that the curves are representative of the transmission function of the monochromator. The solid curve was recorded immediately after new optical elements had been installed,[8] while the dashed curve was measured four months later.[9] Clearly, the flux above the carbon K edge dramatically decreases with time which is attributed to carbon contamination buildup on the reflecting Pt or Au coated optical surfaces when they are exposed to synchrotron radiation.[10] The contamination does not only diminish the photon flux above ~280 eV but also the spectral purity is affected since the scattered light content increases. Thus, measurements in the spectral range 300–1000 eV discussed here can only be carried out if care is taken to avoid carbon contamination on the optical surfaces in the monochromator.

With the availability of sufficiently intense monochromatic radiation, conventional *bulk* absorption measurements still suffer from the fact that the samples have to be in the form of *thin films* (1000–3000 Å) owing to the large absorption coefficients in the soft-x-ray region.[11] Fluorescence detection can, in principle, overcome this problem but fluorescence yields are extremely small ($\sim 10^{-3}$) for low-Z atoms.[12] Detection of the *secondary electron yield* from the sample[8,13] avoids the problem of thin-film samples and allows EXAFS measurements on all vacuum compatible materials. It should be noted that, because of the high-absorption cross sections, EXAFS measurements in the soft-x-ray region need to be carried out in vacuum, anyway, such that the electron yield technique has no disadvantage. One of the most important advantages of the electron yield detection technique lies in the fact that it allows the study of low-Z atoms and molecules adsorbed on solid surfaces. Because of the short electron sampling depth inside the solid, the adsorbate signal is sufficiently intense relative to the bulk background to allow the detection of adsorbed monolayers.[13] We shall discuss and employ the electron yield technique here for the study of low-Z atoms in solids and on surfaces.

Besides discussing experimental problems and solutions in obtaining low-Z K-edge EXAFS spectra, the present paper addresses the problem of the reliability of such measurements for *distance* determinations. The accuracy of distance determinations by means of EXAFS is intimately connected with the knowledge of the scattering phase shift of the outgoing photoelectron.[1] For high-Z atoms, it has been shown by Citrin, Eisenberger, and Kincaid[14] that the EXAFS phase shift is determined by the potential of the *core* electrons in the absorbing and the backscattering atoms resulting in the important concept of phase-shift transferability. Lee and Beni[15] have used this concept and shown that their calculated "atomic" phase shifts can be used to determine nearest-neighbor separations to an accuracy of better than 0.02 Å. For low-Z atoms, the valence electrons constitute a significant fraction of the total number of electrons and the question arises whether calculated "atomic" phase shifts (which, to a large extent, ignore valency effects) can be used to determine neighbor separations. Below, we will determine the reliability of calculated phase shifts[15,16] by performing measurements on systems where the neighbor shell separations are known. In such cases, experimental phase shifts can be derived and compared to the calculated ones.

While the *neighbor separations* depend on the phase of the EXAFS oscillations, the *coordination number* is determined by the amplitude of the EXAFS signal. In general, evaluation of the EXAFS amplitude appears to be significantly more difficult than that of the phase. As discussed in detail by Hunter,[17] the amplitudes are more sensitive to experimental techniques (e.g., higher orders), data reduction procedures (e.g., background subtraction), and data analysis (e.g., range or data, window functions). In addition, the transferability of amplitude functions is complicated by many electron effects.[18] The determination of coordination numbers is of fundamental importance in the study of adsorbed atoms or molecules on surfaces. Often, the coordination number is *the* most important parameter which is needed to characterize an adsorbate-substrate complex.[19,20] Unfortunately, surface EXAFS studies often suffer from signal-to-noise problems[19] which again affect the amplitude more than the phase. Below, we will discuss this problem in more detail and illustrate it for the case of oxygen adsorbed on Si (111). It is pointed out that the use of *polarization-dependent* surface EXAFS[20] overcomes some of the above problems, and future studies will greatly benefit from utilizing the polarized nature of synchrotron radiation.

The structure of the paper is as follows. Section II discusses experimental and theoretical aspects of the various variants of electron EXAFS. Experimental details of the measurements and the yield EXAFS spectra of Si_3N_4, SiO_2, and oxygen on Si (111) are discussed in Sec. III. Section IV summarizes the EXAFS analysis procedures employed here with emphasis on bond length and coordination number determinations. Section V

presents a discussion of the bulk EXAFS data in terms of bond lengths and phase shifts and of the surface EXAFS data in terms of bond lengths and the oxygen coordination number. The paper is summarized in Sec. VI, and implications are given for future work.

II. ELECTRON YIELD EXAFS

Because of its general applicability for the study of almost any sample, including amorphous, polycrystalline, and single-crystal materials or liquids, and its potential for surface studies, electron yield spectroscopy is the technique of choice for EXAFS measurements in the soft-x-ray region.[13] Here, we have used the term "electron yield spectroscopy" in a very general sense. Depending on the kinetic energy of the collected electrons, several different techniques may be distinguished. Let us discuss the various techniques below and illustrate them by means of an example.

In Fig. 2, we show the energy-level diagram for a hypothetical sample consisting of O and Si atoms. The goal is to measure the EXAFS spectrum above the O K edge for this system. The energy levels of the O and Si atoms are shown on the left-hand side and are characterized by their binding energy (E_B) relative to the Fermi level (E_F).[21] At a photon energy $h\nu$, photoelectrons are emitted from the various shells and the created holes are filled by electrons from lower E_B shells, giving rise to fluorescence x rays and/or Auger electrons. For low-Z atoms, the Auger process dominates[12] and, in the following, we shall therefore ignore the fluorescence channel. The resulting hypothetical photoemission spectrum consisting of photoemission and Auger peaks (only the most prominent ones are shown) is shown in the right lower half of Fig. 2. The electrons are characterized by their kinetic energy (E_k) referenced to the Fermi level. The schematic photoemission spectrum shown in the lower right half incorporates the effect of inelastic electron scattering in the solid which leads to an increasing background with decreasing kinetic energy. For illustration purposes, the photoemission spectrum of SiO_2 at $h\nu = 700$ eV is shown in Fig. 3 for kinetic energies exceeding 50 eV.

The O K-edge EXAFS spectrum can be obtained by measurement of the *total* electron *yield*. In this case, all electrons emitted from the sample are collected. This technique to measure x-ray absorption was first used by Lukirskii and coworkers in 1964[22] and later by Gudat and Kunz[23] and Gudat.[24] The latter authors used synchrotron radiation to demonstrate for a variety of samples (metals, semiconductors, and insulators) that, at

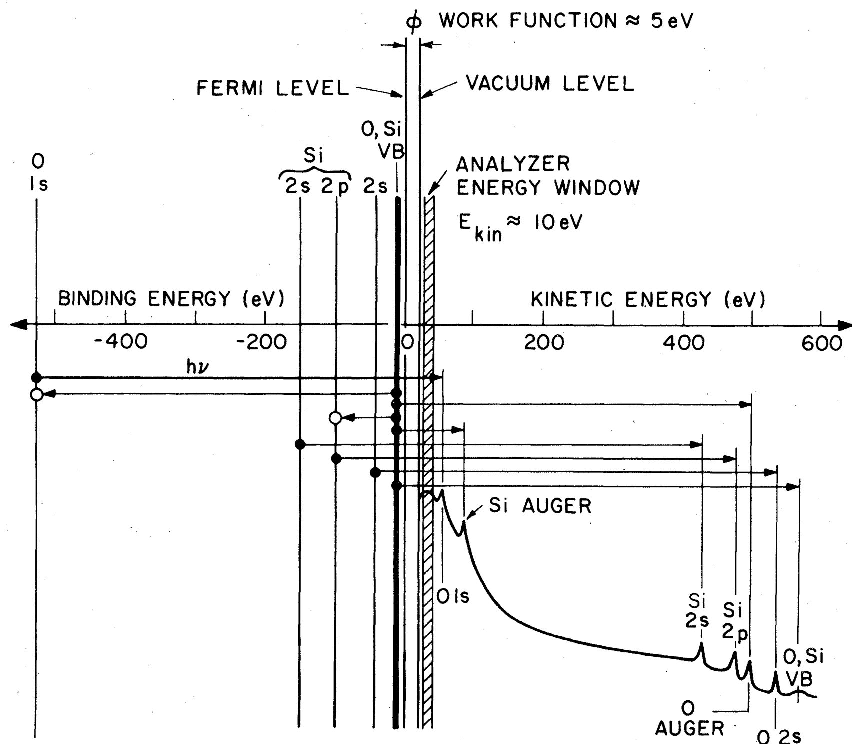

FIG. 2. Energy level diagram for a hypothetical sample consisting of Si and O atoms (left-hand side) and schematic photoemission spectrum at energy $h\nu$ (right-hand side). The approximate positioning of the photoelectron analyzer energy window used in the present experiments is also shown.

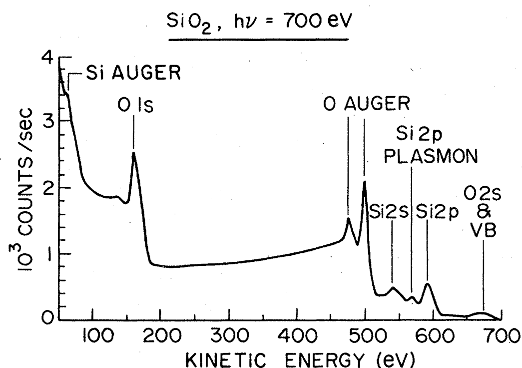

FIG. 3. Photoemission spectrum of a SiO_2 sample at $h\nu = 700$ eV obtained with the grasshopper monochromator.

sufficiently high photon energies ($\gtrsim 50$ eV), the total yield γ is directly proportional to the absorption coefficient μ. This has recently been verified by Martens *et al.*[25] in the hard-x-ray region. Since x rays are absorbed by matter primarily through the photoelectric effects, the number of electrons γ (elastic photoelectrons, elastic electrons originating from recombination processes, and inelastically scattered electrons) created in a depth L of the sample is proportional to the number of absorbed photons $\gamma \sim 1 - e^{-\mu L} \approx \mu L$ for $\mu L \ll 1$. At sufficiently high photon energies ($\gtrsim 50$ eV), the x-ray absorption length $1/\mu$ will always be much larger than a typical electron escape depth L such that the relation $\gamma \sim \mu L$ is valid.

Under some simplified assumptions, the total yield γ can be expressed as[24]

$$\gamma(h\nu) = f(h\nu) g(\phi) [1 - R(\theta, h\nu)] \mu(h\nu) L / \sin\theta_r . \qquad (1)$$

Here, $f(h\nu)$ is a smoothly varying function with photon energy (roughly proportional to $h\nu$),[26] $g(\phi)$ is a material-dependent function which increases with decreasing work function ϕ, $R(\theta, h\nu)$ is the energy dependent reflectivity at an incidence angle θ from the surface, $\mu(h\nu)$ is the absorption coefficient, and $\theta_r \approx \theta$ the angle of the refracted x-ray beam from the surface.[27] The parameter L is an effective electron escape depth[24,28] which depends on the details of the cascading process of the hot primary electrons inside the solid. Its calculation is difficult since it is a complicated sum of electron scattering lengths. However, experiments on a variety of solids[24] have shown that in the soft-x-ray region L usually does not exceed about 50 Å for metals and semiconductors. In insulators, larger values of L are possible because electron-electron scattering is less effective at low kinetic energies.[29]

At x-ray incidence angles which are larger than the angle of total reflection,[30] $R(\theta)$ is negligibly small and, according to Eq. (1) any structure in the yield $\gamma(h\nu)$ arises from the absorption coefficient $\mu(h\nu)$. Because of the small L values, electron yield measurements like other low-energy electron techniques (e.g., LEED, Auger, or photoemission) exhibit a high surface sensitivity.

Measurement of the secondary inelastic (low energy) portion of the total yield is another variation of the electron yield technique.[31] Such measurements are very convenient in practice since they are performed with a conventional electron energy analyzer as used for photoemission.[8,31] The energy window of the analyzer is positioned in the inelastic tail of the photoemission spectrum, typically $E^* \lesssim 5$ eV above the vacuum level (i.e., $E_k \lesssim 10$ eV above E_F). This case is shown in Fig. 2 since all measurements reported below were carried out in this mode. We will refer to such measurements as *partial yield* or *secondary yield* spectra. Since, at the photon energies considered here, the number of elastically emitted Auger and photoelectrons is negligible as compared to the number of inelastically scattered ones, the secondary and total yield spectra will be identical. For both techniques, the O K edge is observed because the O KVV Auger channel opens up at the threshold of the O 1s transition, giving rise to elastic and, more important, *inelastically* scattered Auger electrons. As seen from Fig. 2, the O 1s core line will be swept through the analyzer window at an energy $E_k = (E^* + \text{work function})$ above threshold. However, for small values of E_k, the O 1s transition strength will still be small,[32] and the photoemission intensity will be negligible as compared to the large intensity of the inelastic tail. *Therefore, in practice, the secondary yield spectrum does not deviate from the total yield spectrum*. In general, a secondary yield EXAFS measurement above a certain absorption edge can be successfully carried out as long as no other absorption edge of the sample under investigation lies in the EXAFS energy range above the primary edge. This criterion is the same as for standard absorption experiments carried out in transmission.

A third variant of electron yield spectroscopy consists of detecting the elastically emitted *Auger* intensity corresponding to the core excitation of interest.[19,33] This technique makes use of the fact that the probability of creating a core hole (i.e., the absorption coefficient) is proportional to either the probability of filling it by a radiative (i.e., x-ray fluorescence) or a nonradiative (i.e., Auger electrons) transition. Because the signal from the atom of interest is measured directly in an Auger or fluorescence EXAFS measurement, much higher signal-to-noise ratios are obtainable

than in a conventional transmission EXAFS experiment and surface EXAFS experiments in the Auger detection mode have been carried out by Citrin, Eisenberger, and Hewitt.[19] For the study of surface related phenomena, the Auger technique offers an advantage over the fluorescence technique[34] in that it is more surface sensitive due to the shorter electron[28] than photon[11] scattering length in solids.

For the O–Si system, an Auger EXAFS experiment above the O K edge consists of detecting the O Auger electrons at ~500 eV (KVV) or ~480 eV (KLV) (compare Fig. 3).[35] However, it can be seen from Fig. 2 that with increasing photon energy the Si 2s and Si 2p photoemission lines and their loss structure will be swept through the electron analyzer window which remains fixed at the kinetic energy of the O Auger line. This effect is visible in Fig. 4 which shows the Auger EXAFS ($E^* = 498$ eV) spectrum of a monolayer of oxygen on Si (111). Above the O K edge at ~535 eV and the first EXAFS peak at ~555 eV, the count rate increases steeply to a peak at ~600 eV followed by other less intense peaks. As indicated in Fig. 4, these latter peaks arise from the Si 2p, the Si 2p plasmon loss, and the Si 2s photoemission peaks which successively fall into the analyzer window as the photon energy is increased (compare Fig. 2). The strength of these EXAFS unrelated structures precludes the possibility of normalizing them out reliably. The present example points out one of the weaknesses of the Auger EXAFS techniques. Especially in the soft-x-ray region, Auger EXAFS spectra will often be obscured by structures arising from photoemission peaks.

Often, it is advantageous to make use of certain sophistications of the total yield, partial yield, or

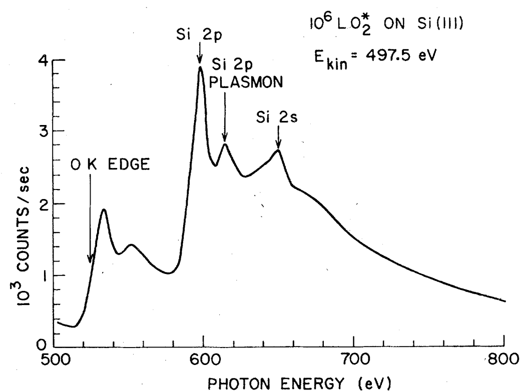

FIG. 4. Auger yield spectrum of about one monolayer oxygen on Si (111) in the photon energy range above the O K edge. The electron analyzer window was positioned in the O KVV Auger line.

Auger yield technique. For example, the surface sensitivity can be enhanced by collecting only electrons at grazing *emission angles*.[36] In practice, this is most effective for the Auger yield since refraction of electrons at the surface is only well defined for elastically emitted electrons.[37] For inelastically emitted electrons, expecially at low kinetic energy, a grazing electron propagation direction outside the crystal cannot necessarily be related to a grazing (and therefore surface enhancing) propagation inside the crystal. The total and partial electron yields are largest for x-ray *incidence angles* slightly larger than the angle of total reflection,[25,38] and this geometry should be chosen for all cases where the polarization dependence[20,39] of the EXAFS is unimportant or cannot be exploited (e.g., amorphous or polycrystalline materials). The positioning of the *energy window* in partial yield measurements is a parameter which can be used to increase the surface sensitivity. By positioning the energy window at higher kinetic energy, inelastic electrons are detected which have undergone fewer scattering events resulting in a shorter effective escape depth L and hence a reduced bulk background signal. In our example shown in Fig. 2, the analyzer window could be set around 380 eV, just below the kinetic energy at which the Si 2s electrons ($E_B \sim 150$ eV) emerge from the sample at the O 1s threshold ($h\nu \sim 535$ eV). In this case, the O K-edge absorption is observed through inelastically scattered O Auger electrons only. Since Auger electrons are emitted with the same kinetic energy, the ratio of elastically emitted to inelastically scattered electrons is constant. Thus, the intensity of inelastically scattered Auger electrons will exhibit the same EXAFS modulations as the elastically emitted intensity. At this point, it is interesting to note that the *elastic photoemission intensity* (i.e., the O 1s intensity in our example) will, in general, not exhibit the same modulations as the absorption coefficient.[40-42] Since the elastic photoelectrons are emitted with increasing kinetic energy as the photon energy is increased, both the angular distribution as well as the fraction of electrons lost in inelastic scattering events may change. Only in the limit of complete angular averaging and a smoothly varying electron-loss function would one expect a correspondence (except for the central atom phase-shift term[41]) between the modulations of the elastic photoemission intensity and those of the absorption coefficient.

The optimum choice among the various variants of electron yield spectroscopy depends on the specific sample under investigation. The total and partial yield techniques are applicable in the majority of cases, and they are well suited for

the study of most bulk materials. For the study of surface effects, the Auger technique will, in general, provide the most sensitivity, but its applicability is much more limited, especially in the most interesting soft-x-ray region.

III. EXPERIMENTAL YIELD SPECTRA

A. Experimental details

Experiments were carried out on the 4° beam line at SSRL which is equipped with the grazing incidence monochromator grasshopper.[7] At the time of the present experiments, a 600 l/min grating was installed yielding a constant spectral bandwidth of ~0.2 Å. With SPEAR operating at 2.0 GeV and ~10 mA, the photon flux in the 400–1000 eV range was about $(0.5-1)\times 10^9$ photons/sec. The transmission function of the monochromator had an energy dependence intermediate to the two curves shown in Fig. 1. The p-polarized light ($\vec{E}$ vector in plane spanned by the sample normal and the Poynting vector) was incident on the samples at grazing angles of about 10°. The samples were positioned in the focal point of a double-pass cylindrical mirror analyzer (CMA).[43] Electrons were collected at an energy $E^* = 3$ eV above the vacuum level. The analyzer window width (energy resolution) was adjusted between about 0.4 and 1.6 eV such that the count rate was around 10^5 counts/sec. Yield spectra were recorded in typically 1 h. The count rate was limited by the channeltron electron multiplier in the CMA which needs to be operated such that the count rate varies linearly with the number of incident electrons. With more efficient detectors or detection techniques, higher count rates could be obtainable. The experiments were carried out in ultrahigh vacuum (UHV) at a base pressure of $<3\times 10^{-10}$ torr.

The Si_3N_4 and SiO_2 samples were cleaned in situ by Ar^+ bombardment in order to remove surface contamination. A clean Si (111) face was obtained by in situ cleaving a Si single crystal. In the present studies, oxidation was performed by introducing pure oxygen into the sample chamber to a certain partial pressure while leaving the ionization gauge on. As discussed previously,[44] this procedure produces excited oxygen (to be denoted $O_2{}^*$) which is more reactive.

B. Normalization of spectra

As seen from Fig. 1, the flux emerging from the monochromator exhibits sharp structures at the K and L absorption edges of contaminants on the reflecting optical surfaces. The normalization of the measured electron yield intensity to these modulations of the incident photon flux is a difficult problem in the soft-x-ray region. Ideally, one would like to have a beam monitor which (i) provides an output signal proportional to the number of incident photons, (ii) has a constant quantum efficiency over the investigated energy region, (iii) operates without a significant loss in transmitted intensity, and (iv) does not introduce any intensity modulations in the transmitted beam. We have resorted to a technique which relies on the stability of the photon flux emitted by the storage ring SPEAR over the time of a measurement. Tests showed that the flux emerging from the grazing incidence monochromator was remarkably stable and typically did not deviate by more than ±0.2% from the mean exponential decay curve. The transmission function of the monochromator can then be determined by measuring the yield spectrum γ_R^* of a reference sample which does not have any absorption edges in the photon energy range of interest. Since, in this case, the quantum efficiency of the reference detector (i.e., the normalized yield) γ_R which is proportional to the absorption coefficient μ_R [see Eq. (1)] is a smooth function with photon energy, any structure in $\gamma_R^* = \gamma_R N(h\nu)$ will be due to the monochromator transmission function $N(h\nu)$. Dividing the yield EXAFS spectrum of the sample under investigation by γ_R^* will eliminate any structure in the incident photon flux. This point is illustrated in more detail in Ref. 13.

In order to extract all information contained in the EXAFS, it is necessary to first remove the background originating from *preedge absorption* processes which underlies the absorption structure of interest. This is usually not essential if one is only interested in extracting bonding distances since these depend on the *position* of the EXAFS interference maxima and minima. However, the removal of the background due to preedge absorption processes is crucial when information contained in the EXAFS amplitude (e.g., coordination numbers) is being sought.[17] Usually, the preedge absorption is extrapolated over the pastedge energy region of interest and then subtracted out. This procedure requires knowledge of the preedge absorption over an energy range which is approximately as long as the EXAFS data range.[17] In the soft-x-ray region, this is often difficult because of closely spaced absorption edges. We have used a different procedure.

For low-Z atoms on surfaces or in solids, the main portion of the preedge absorption will, in general, originate from the heavier atoms constituting the substrate or the neighbors. For the systems investigated here, the dominant preedge background originates from the Si $L_{2,3}$ (~100 eV) and Si L_1 (~150 eV) absorption. Thus, by subtracting the yield spectrum of a clean Si sample from that of the sample under investigation, the

preedge background can be eliminated. Of course, the two spectra have to be normalized to the same yield before the absorption edge. The background-corrected and flux-normalized yield spectrum γ is thus obtained from the unnormalized yield spectrum γ^* and the unnormalized reference (i.e., Si) yield spectrum γ_R^* as

$$\gamma = (\gamma^* - \gamma_R^*)/\gamma_R^* . \qquad (2)$$

The so-obtained normalized yield spectrum γ will deviate from the corresponding absorption coefficient μ only by a slowly varying function $c(h\nu)$, i.e., $\gamma = c\mu$. The function $c(h\nu)$ incorporates intrinsic differences between the normalized yield and the absorption coefficient [cf. Eq. (1)] as well as a factor ($\sim 1/\gamma_R$) which arises from the special normalization procedure employed. However, the function $c(h\nu)$ is eliminated when the final EXAFS signal

$$\chi = (\mu - \mu_0)/\mu_0 = (\gamma - \gamma_0)/\gamma_0$$

is computed where γ_0 or μ_0 is a smooth background function which is fit through the oscillatory structure above the absorption edge. We have found spline-polynomial functions, typically two or three polynomials of first or second order, to give good results.

C. Silicon nitride

The normalized yield spectrum of Si_3N_4 is shown in Fig. 5(a). The sample was prepared by chemical vapor deposition (CVD) onto a Si substrate. The spectrum exhibits a strong absorption spike ("white line") at the N K edge (~400 eV) and several pronounced EXAFS wiggles above the edge. White lines often occur at the threshold of $L_{2,3}$ absorption edges and are usually attributed to a high density of d-like states in the conduction band just above the Fermi level.[45,46] In the present case, the white line is attributed to excitonic effects or, more probable, to a high p-like density of states at the conduction band bottom. The predominant p-like character of the lower conduction band arises from both Si sp^3 hybrids and N $2p$ states similarly as discussed by Pantelides and Harrison for SiO_2.[47]

The EXAFS signal $\chi = (\gamma - \gamma_0)/\gamma_0$ obtained from Fig. 5(a) is shown in Fig. 5(b). Now, the oscillations at higher photon energy are clearly visible. Both spectra in Fig. 5 exhibit a small and narrow peak around 535 eV which is attributed to the K edge of a residual-oxygen contamination on the surface of or within the Si_3N_4 sample. However, since its amplitude and width are much smaller than that of the EXAFS oscillations, its effect on the Fourier transform will be negligible.

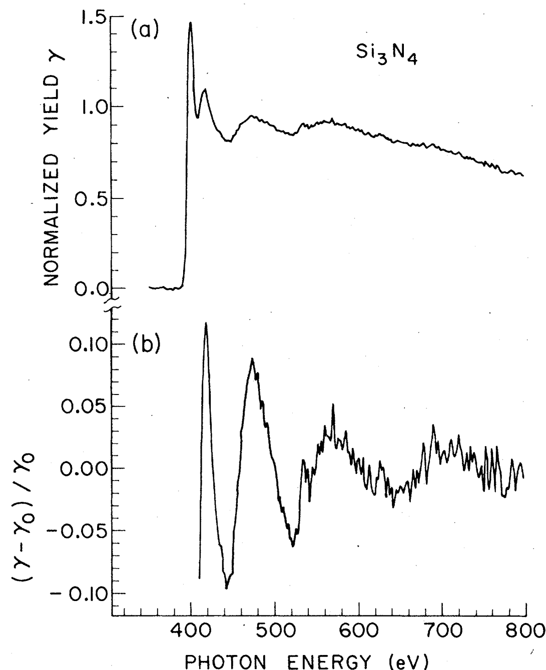

FIG. 5. (a) The normalized secondary yield spectrum of *CVD* Si_3N_4. (b) The EXAFS oscillations obtained from (a) after background subtraction.

D. Silicon oxide

Figure 6(a) shows the normalized yield spectrum of a sample of SiO_2 thermally grown on Si to a thickness of about 500 Å. Similar to the N K-edge spectrum shown in Fig. 5(a), the O K-edge absorption exhibits a pronounced spike at the edge, as expected, and several oscillations of decreasing magnitude at higher energies. The threshold structure in the energy range up to 570 eV closely resembles that previously reported in transmission by Ershov and Lukirskii.[48] The EXAFS oscillations obtained after subtraction of a smooth spline function are shown in Fig. 6(b).

E. Oxygen on Si (111)

We have performed surface EXAFS measurements on one of the initial oxidation stages of a Si (111) 2×1 surface. As shown in Fig. 7, the particular surface oxide under investigation is characterized by a Si $2p$ chemical shift of ~2.5 eV. This oxidation stage has been observed by others,[49-51] and it can be produced by exposing a clean Si (111) surface to 10^6 L of excited oxygen O_2^*. The secondary yield spectra of a clean Si (111) crystal and after exposure to 10^6 L O_2^* are shown in Fig. 8(a). The structure in the clean Si (111) yield spectrum is due to oxygen contamination on the optical elements of the monochro-

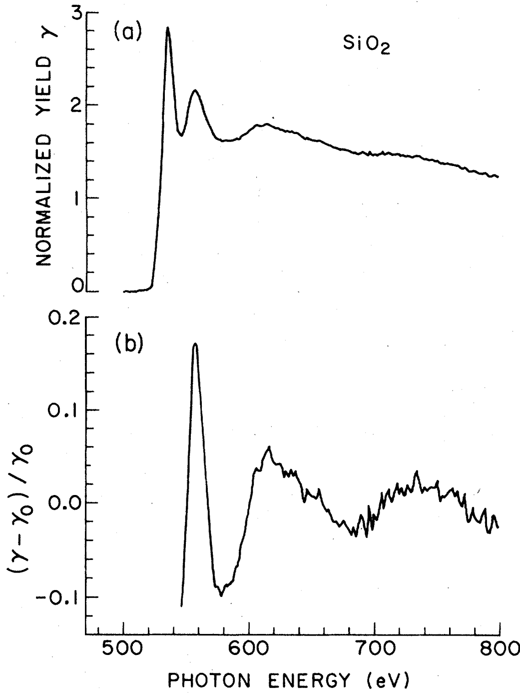

FIG. 6. (a) The normalized secondary yield spectrum of thermally grown SiO_2 on Si. (b) The EXAFS oscillations obtained from (a) after background subtraction.

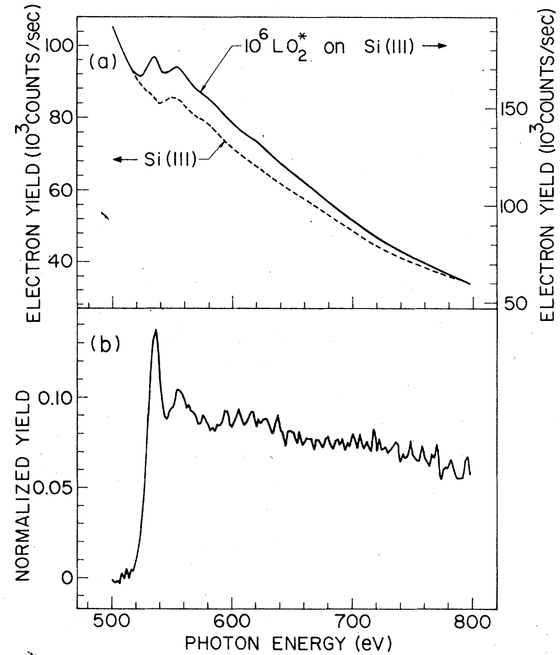

FIG. 8. (a) Secondary yield spectra from clean Si (111) and after adsorption of oxygen (same sample as for Fig. 7). (b) Normalized secondary yield spectrum obtained from (a) by a procedure discussed in the text.

mator. The normalized yield spectrum in Fig. 8(b) clearly exhibits the O K edge (~530 eV) and three EXAFS oscillations above the white line at threshold. The noise in the spectrum is mainly due to counting statistics but has a small contribution from instabilities of the electron beam in SPEAR. The spectra in Fig. 8(a) [and hence the spectrum in Fig. 8(b)] were recorded in about two hours total.

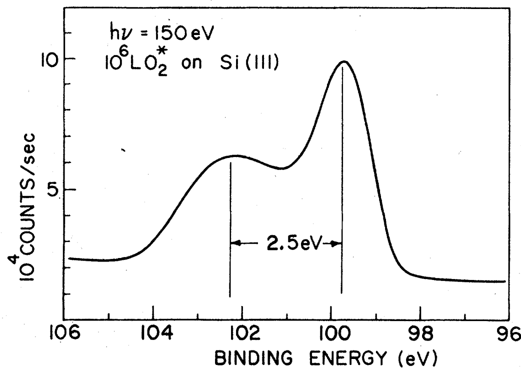

FIG. 7. Photoemission spectrum in the Si $2p$ region at $h\nu = 150$ eV for a particular stage of oxidation corresponding to a chemical shift of the Si $2p$ line of 2.5 eV (left peak) from that in clean Si (right peak).

IV. DETERMINATION OF PHYSICAL PARAMETERS

A. EXAFS formalism

The EXAFS for the case of K-shell absorption is given by[1,52]

$$\chi(k) = \frac{\mu - \mu_0}{\mu_0} = \sum_i A_i(k) \sin[2kr_i + \phi_i(k)], \qquad (3)$$

where the conversion from energy (eV) to wave vector (Å^{-1}) scale is given by

$$k = 0.5123(h\nu - E_0)^{1/2}. \qquad (4)$$

Here, E_0 is the "zero" of the EXAFS energy scale to be discussed below. The summation in Eq. (3) is over neighbor shells i separated from the absorbing atom by a distance r_i. $\phi_i(k)$ is the total phase shift which we write[16]

$$\phi_i(k) = \phi_a(k) + \phi_b(k) - \pi. \qquad (5)$$

Here, $\phi_a = 2\delta_1$ is the $l = 1$ phase shift of the central atom and ϕ_b is the phase of the backscattering amplitude. In the case where the neighbor shell i consists of identical atoms, the total amplitude $A_i(k)$ in Eq. (3) is given by

$$A_i(k) = (N_i^*/kr_i^2)F_i(k)e^{-2\sigma_i^2 k^2} e^{-2r_i/\lambda(k)}, \qquad (6)$$

where the sign of $A_i(k)$ is chosen consistently with

Eq. (5) to make the backscattering amplitude $F_i(k)$ positive. The exponential terms in Eq. (6) are the Debye-Waller factor-like term[53] and the damping term due to inelastic scattering [mean free path $\lambda(k)$] of the photoelectrons. N_i^* is the effective coordination number of the central atom at distance r_i (ith shell) and is given by[41]

$$N_i^* = 3 \sum_j^{N_i} \cos^2\theta_j . \quad (7)$$

Here, the sum extends over all neighbor atoms j (total number N_i) in the ith shell and θ_j is the angle between the electric field vector $\vec{E}$ of the x rays at the central atom site and the vector $\vec{r}_{ij}$ from the central atom to the jth atom in the ith shell. For polycrystalline or amorphous materials, an average over all angles yields $N_i^* = N_i$ such that the *effective* coordination number N^* is equal to the *real* coordination number N. For single-crystal materials, or in the case of oriented molecules or atoms on surfaces, Eq. (7) has to be evaluated for an assumed model geometry.

The thermal correlation factor σ_i in Eq. (6) is given by[39,53]

$$\sigma_i^2 = \frac{2\hbar}{NM} \sum_{\vec{q}l} \frac{1}{W_{\vec{q}l}} (\hat{r}_{ij} \cdot \hat{e}_{\vec{q}l})^2 (n_{\vec{q}l} + \tfrac{1}{2}) \times (1 - \cos\vec{q} \cdot \vec{r}_{ij}) , \quad (8)$$

where N is the number of atoms of mass M, $\hat{e}_{\vec{q}l}$ is a unit polarization vector for phonons of momentum $\vec{q}$, polarization l, frequency $W_{\vec{q}l}$, and occupation number $n_{\vec{q}l}$. The unit vector $\hat{r}_{ij}$ points in the directions of $\vec{r}_{ij}$. The important point about Eq. (8) is that the EXAFS amplitude is preferentially sensitive to vibrations along the interatomic axis. Especially in surface EXAFS experiments, this could be exploited to aid in determining the correct structural model.

B. Bond lengths and phase shifts

For the determination of bonding distances r_i or to obtain the phase shift $\phi_i(k)$, it is convenient to use the Fourier transform technique.[1] In order to obtain r_i for an unknown system, $\phi_i(k)$ has to be known or vice versa. The phase shift $\phi_i(k)$ is either obtained from a *calculation*[15,16] or derived from a *standard*[54] consisting of the same atoms as the system under investigation. In the latter case, the phase shift is simply obtained by Fourier transforming the EXAFS spectrum $\chi(k)$ of the standard

$$f(r) = \frac{1}{2\pi} \int_{k_{\min}}^{k_{\max}} \chi(k) k^n e^{-i2kr} \, dk , \quad (9)$$

where $1 \leq n \leq 3$ and $k_{\min}$ and $k_{\max}$ are the minimum and maximum wave vectors, respectively, of the usable experimental data. In general, $k_{\min}$ and $k_{\max}$ should be chosen to coincide with a node of $\chi(k)$ in order to eliminate termination errors. It is convenient to use a suitable window function for this purpose.[15] The function $f(r)$ will exhibit peaks corresponding to various neighbor shells i. Since in the standard the separation from the central atom A to a given neighbor shell consisting of atoms B is accurately known, the corresponding peak can easily be identified and it can be filtered out from the total transform by a window function. The filtered peak in r space is then back transformed into k space using the complex Fourier transform yielding a complex function of general form

$$\chi'(k) k^n = \int_{r_1}^{r_2} f(r) e^{i2kr} \, dr \quad (10a)$$

$$= A'(k) e^{i\zeta(k)} , \quad (10b)$$

where R is the distance between atoms A and B in the standard. The phase shift $\phi(k)$ corresponding to scattering between atoms A and B is obtained by subtracting $2kR$ from the total phase $\zeta(k)$. Note that Eq. (10) also provides the amplitude $A'(k)$ of the EXAFS signal corresponding to a known number of neighbor atoms B. Assuming the transferability of phase shifts,[14] the derived phase shift $\phi(k)$ can then be used for another system consisting of atoms A and B for which the bonding distances are unknown.

In order to determine neighbor shell separations by means of the Fourier-transform technique, we can eliminate the phase shift and the amplitude dependence on k before we transform, i.e.,[15]

$$F(r) = -\frac{1}{2\pi} \int_{k_{\min}}^{k_{\max}} \left(\frac{\chi(k) k^n e^{-i\phi(k)}}{A(k)} \right) e^{-i2kr} \, dk . \quad (11)$$

Here, the minus sign arises from our definition of the phase shift [factor π, see Eq. (5)]. In Eq. (11), we have assumed that the phase shift $\phi(k)$ and amplitude $A(k)$ are known from a calculation or from a standard, i.e., we have assumed transferability of both quantities.[14-16] As seen from Eq. (6), only the backscattering amplitude $F_i(k)$ can cause a nonmonotonic k dependence of the total amplitude $A(k)$.[55] Therefore, it is sufficient to use $F_i(k)$ instead of $A(k)$ in Eq. (11).

As discussed by Lee and Beni,[15] the imaginary part of $F(r)$ is a symmetric function peaked at the neighbor distance and should coincide with the peak of the absolute value $|F(r)|$ of the transform. The condition that $\mathrm{Im}F(r)$ and $|F(r)|$ should peak at the same distance can be used to eliminate the problem of choosing the "zero" of the EXAFS en-

ergy scale. By allowing E_0 to be adjustable by several eV in order to align the peaks in Im$F(r)$ and $|F(r)|$, one can correct for the neglect of valence effects in transfering the phase shift. A change of E_0 by ΔE_0 (in eV) causes a change in the momentum scale from k (in Å^{-1}) to[15]

$$k' = (k^2 - 0.2625\Delta E_0)^{1/2} \quad (12)$$

and the phase shift function changes to

$$\phi'(k') \approx \phi(k) + 0.2625\Delta E_0 R/k\,, \quad (13)$$

where R is the distance of the neighbor involved.

An alternate method to reliably determine bonding distances has been discussed by Martens *et al.*[56] In their method, the total EXAFS signal is transformed according to Eq. (9) and the filtered-neighbor-shell peak of interest is backtransformed to yield a complex function as in Eq. (10). Subtraction of a predetermined phase shift $\phi(k)$ from the total phase $\zeta(k)$ and division by $2k$ should give a constant ($=R$) for all k values. Deviations from the constant functional form are minimized by adjusting E_0.

C. Amplitudes

The total amplitude function $A_i(k)$ given by Eq. (6) contains information on several parameters. For our purposes, we will take the point of view that the backscattering amplitude function $F_i(k)$ can be calculated and is chemically transferable[15,16] and that the mean free path λ can be obtained from photoemission data.[28] Then, the total EXAFS amplitude $A_i(k)$ is determined by the effective coordination number N_i^* and the effective mean-square displacement σ_i^2. As discussed by Stern, Sayers, and Lytle,[54] the quantities N_x^* and σ_x^2 for a given shell in a sample under investigation can be obtained by comparison of its amplitude $A_x(k)$ with that of a standard [with quantities N_s^*, σ_s^2, and $A_s(k)$]. From Eq. (6), we obtain

$$\ln(A_s(k)/A_x(k)) = \ln(N_s^* r_x^2/N_x^* r_s^2) + 2k^2(\sigma_x^2 - \sigma_s^2)\,, \quad (14)$$

where we have omitted the term $2(r_x - r_s)/\lambda(k)$ which is negligible because

$$2|r_x - r_s| \approx 0.1 \text{ Å} \ll \lambda(k) \approx 5 \text{ Å}.$$

A linear plot of $\ln[A_s(k)/A_x(k)]$ vs k^2 yields the unknown coordination number N_x^* from the ordinate intercept at $k=0$ and σ_x^2 from the slope.

V. DATA ANALYSIS AND DISCUSSION

A. Bulk EXAFS

Here, we discuss the analysis of the bulk Si_3N_4 and SiO_2 data with emphasis on bonding distance determinations. There are three main differences as compared to previously reported EXAFS spectra in the hard-x-ray ($\gtrsim$4 keV) region. (i) The present data are recorded by electron yield detection rather than in transmission or fluorescence (ii) the present EXAFS energy range above the absorption edge is shorter (250–400 eV) than in previously reported studies (>500 eV), and (iii) the reliability of calculated phase shifts is unknown since no comparison to experimentally derived ones exists. For the above reasons, it is necessary to first establish reliability limits for the parameters of interest.

The EXAFS signal $\chi(k)\,k$ for Si_3N_4 obtained from Fig. 5(b) by means of Eq. (4) is shown in Fig. 9(a). Here, E_0 was chosen 6 eV above the inflection point of the absorption edge in order to align $|F(r)|$ and Im$F(r)$ as shown in Fig. 9(b). The Fourier transform $F(r)$ was obtained according to Eq. (11) using calculated values for $\phi(k)$ and $A(k)$.[16]

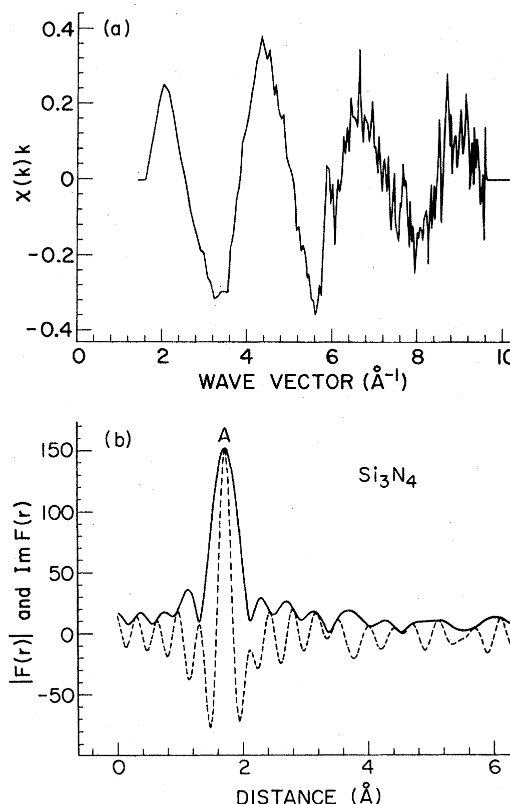

FIG. 9. (a) EXAFS signal $\chi(k)\,k$ for Si_3N_4 as a function of wave vector k obtained from Fig. 5(b) using a value of $\Delta E_0 = 6$ eV [see Eq. (12)]. (b) Absolute value (solid curve) and imaginary part (dashed curve) of the Fourier transform $F(r)$ obtained from (a) using calculated values for the phase shift and backscattering amplitude as discussed in the text.

Since the central atom phase-shift calculation is only expected to be reliable for $k \gtrsim 4$ Å^{-1},[16] we have extrapolated the calculated phase shifts to smaller k values by fitting a second-order polynomial in k in the region 4 Å$^{-1} \leq k \leq 14$ Å^{-1}. The transform for Si_3N_4 in Fig. 9(b) is dominated by a single peak A at 1.705 Å which corresponds to the N–Si nearest-neighbor separation. There are no significant contributions from more distant shells. For crystalline α-Si_3N_4, the second-nearest-neighbor shell consisting of 11 N atoms falls at a mean separation of 2.87 Å.[57] We do not observe this shell probably because of the largely amorphous character of CVD Si_3N_4 studied here.

The EXAFS oscillations $\chi(k)\,k$ for SiO_2 are shown in Fig. 10(a). In this case, E_0 falls 10 eV above the inflection point of the O K edge when $|F(r)|$ and Im$F(r)$ are aligned as shown in Fig. 10(b). The Fourier transform exhibits two peaks A and B above the noise level which are attributed to the first (O–Si) and second (O–O) neighbor shell separations. Using calculated values for $\phi(k)$ and $A(k)$ for the O–Si and O–O scattering cases, peaks A and B fall at 1.585 and 2.57 Å, respectively. It is interesting to note that, when the maxima of $|F(r)|$ and Im$F(r)$ are aligned for peak A (using O–Si parameters), they are shifted considerably with respect to each other for peak B (see Fig. 10) and *vice versa* using parameters for the O–O scattering case. This is direct evidence that peaks A and B are due to different atomic species in the corresponding neighbor shells.

Results for the derived bond lengths in Si_3N_4 and SiO_2 are summarized in Table I where they are compared to those determined from other diffraction experiments. For the next-nearest-neighbor shell, the bond lengths derived from the present EXAFS data are within 0.025 Å of those determined by other means. In both cases, the EXAFS bond lengths are *shorter*. Figure 11

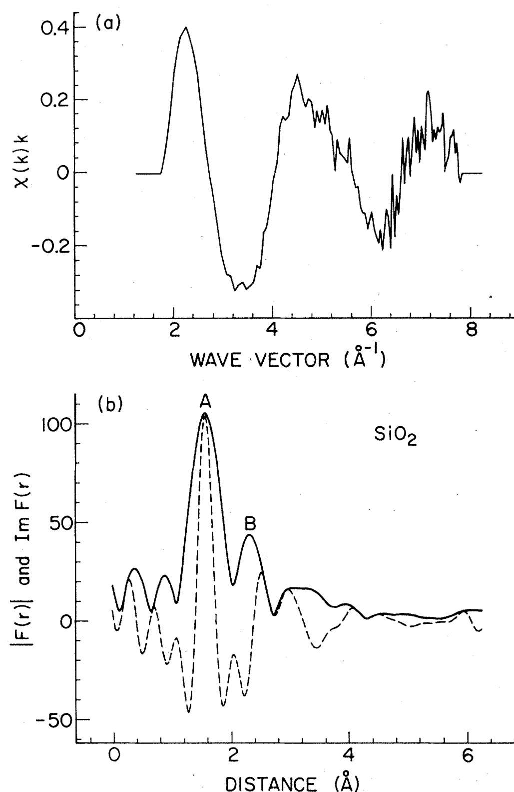

FIG. 10. (a) EXAFS oscillations $\chi(k)\,k$ for SiO_2 as a function of wave vector k obtained from Fig. 6(b) with $\Delta E_0 = 10$ eV [see Eq. (12)]. (b) Absolute value (solid curve) and imaginary part (dashed curve) of the Fourier transform $F(r)$ obtained from (a) using calculated values for the phase shift and backscattering amplitude for the O–Si system as discussed in the text.

shows a plot of the dervied N–Si neighbor distance as a function of wave vector using the method of Martens *et al.*[56] The distance $R(k)$ plotted in Fig. 11 was obtained from the relation

$$R(k) = [\zeta(k) - \phi(k)]/2k\,, \qquad (15)$$

TABLE I. Comparison of derived with tabulated bond lengths.

	Neighbor	Number of neighbors	Nearest-neighbor separation R_D (Å)	EXAFS neighbor shell separation[c] R_E (Å)	ΔR[d] (Å)
Si_3N_4	Si	3	1.72 ± 0.02[a]	1.705 ± 0.02	0.015
SiO_2	Si	2	1.61 ± 0.02[b]	1.585 ± 0.03	0.025
	O	6	2.62 ± 0.03[b]	2.57 ± 0.05	0.05

[a] R. W. G. Wyckoff, *Crystal Structures* (Wiley, New York, 1964).
[b] For a review, see, A. C. Wright, Adv. Struct. Diffr. Methods 5, 1 (1974).
[c] Determined using calculated phase shifts.
[d] $\Delta R = R_D - R_E$.

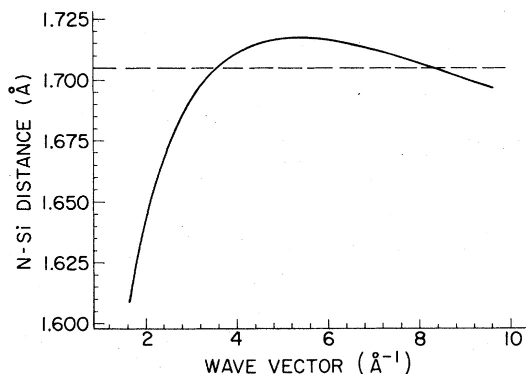

FIG. 11. N–Si nearest-neighbor distance in Si_3N_4 as a function of wave vector using the method of Ref. 56 (solid line). We have used a value of $\Delta E_0 = 6$ eV. The dashed line is the *mean* neighbor distance which is identical to that derived using Lee and Beni's method (Ref. 15 and Fig. 9).

where $\zeta(k)$ is the total phase of the N–Si first-neighbor-shell EXAFS signal [cf., Eq. (10)] and $\phi(k)$ is the calculated phase shift [Eq. (5)]. As before, we have used a value $\Delta E_0 = 6$ eV. Clearly, the mean value for the derived distance (dashed line in Fig. 11) is decreased by the small $R(k)$ values at high and especially low k values. Inspection of Eq. (15) reveals that this is caused by the fact that the calculated phase shifts $\phi(k)$ are too large at high and more important low-k ($\lesssim 4$ Å^{-1}) values. The discrepancy at low-k values is attributed to inadequate treatment of the valence electrons. However, as shown above, the error in the determined nearest-neighbor distance caused by this inadequacy is small ($\lesssim 0.03$ Å). The second-nearest-neighbor distance in SiO_2 derived by EXAFS is 0.05 Å too small. The larger discrepancy for the second as compared to the first-neighbor shell separations has been observed and discussed before.[15] In our case, it could be explained merely by the worsened signal to background (compare Fig. 10).

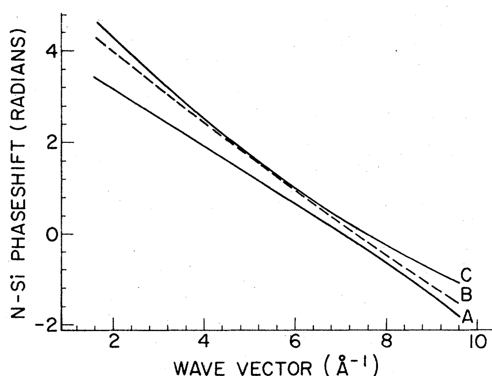

FIG. 12. Comparison of calculated and experimentally derived phase shifts for the N–Si system. The plotted calculated phase shift (curve C) is the sum of the central atom and backscattering phase shifts $\phi_N + \phi_{Si} = 6.322 - 1.085k + 0.0326k^2$. The phase shift curves A and B were derived from experiment by choosing E_0 at the inflection point of the N K edge and assuming $\Delta E_0 = 6$ eV, respectively.

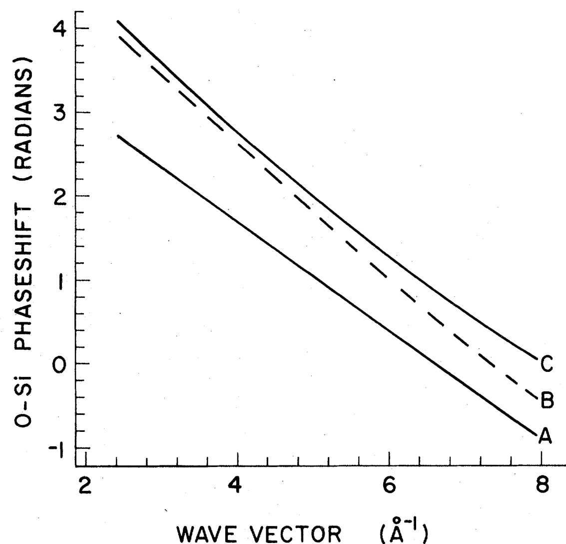

FIG. 13. Calculated and experimentally derived phase shifts for the O–Si system similar to Fig. 12. Curve C is the calculated total phase shift $\phi_O + \phi_{Si} = 6.364 - 1.013k + 0.0273k^2$. For curve A, E_0 coincided with the inflection point of the edge and, for curve B, we used $\Delta E_0 = 10$ eV.

The previous discussion indirectly provides information on the quality of the calculated phase shifts since the error in the determined bond length basically reflects the error in the calculated phase shift. Figures 12 and 13 directly compare the calculated phase shifts (curves C) with experimentally derived ones where we have used the bond lengths derived by x-ray diffraction (Table I). Curves A and B correspond to phase shifts which were obtained by assuming E_0 at the inflection point of the edge or a value ΔE_0 above the edge [see Eq. (13)], respectively. We chose $\Delta E_0 = 6$ eV for Si_3N_4 and $\Delta E_0 = 10$ eV for SiO_2 which were the optimum choices for the *calculated* phase shifts as discussed above. The differences between curves B and C therefore correspond to a change in bond length of 0.015 Å (Si_3N_4) and 0.025 Å (SiO_2). It is interesting to note that the derived phase shifts are very nearly linear in k.

The results discussed in the previous two paragraphs can also be discussed in terms of the concept of phase-shift transferability[14] for low-Z atoms. The fact that calculated "atomic" phase

shifts can be successfully used to obtain bonding distances implies that, at least in the systems studied here, low-Z atom phase shifts are chemically transferable.

B. Surface EXAFS

The EXAFS signal $\chi(k)k$ for 10^6 L O_2* on Si (111) obtained from Fig. 8(b) after background subtraction and conversion into k space is shown in Fig. 14(a). We have used a value of $\Delta E_0 = 11$ eV above the inflection point of the O K edge as the zero of the wave-vector scale. The absolute value and imaginary part of the Fourier transform $F(r)$ of the oscillations in Fig. 14(a) are shown in Fig. 14(b) as solid and dashed curves, respectively. The transform is dominated by a peak denoted A with two weaker peaks at smaller distances ~1 and ~0.4 Å. Using calculated values for $\phi(k)$ and $A(k)$ for the O–Si scattering case, peak A falls at 1.62 Å, a 0.035 Å larger value than for the corresponding peak in SiO_2. Although we assign an

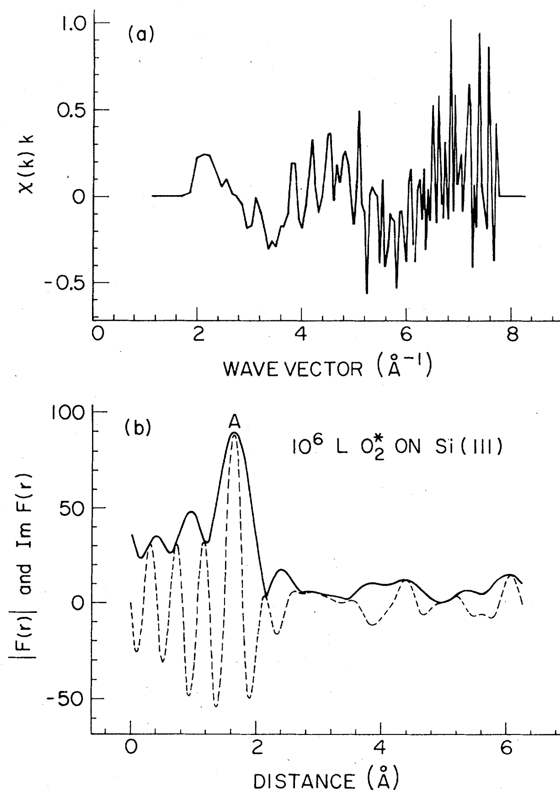

FIG. 14. (a) EXAFS signal $\chi(k)\, k$ for oxygen on Si (111) obtained from Fig. 8(b) using a value of $\Delta E_0 = 11$ eV. (b) Absolute value (solid curve) and imaginary part (dashed curve) of the Fourier transform $F(r)$ obtained from (a) using calculated values for the phase shift and backscattering amplitude as discussed in the text.

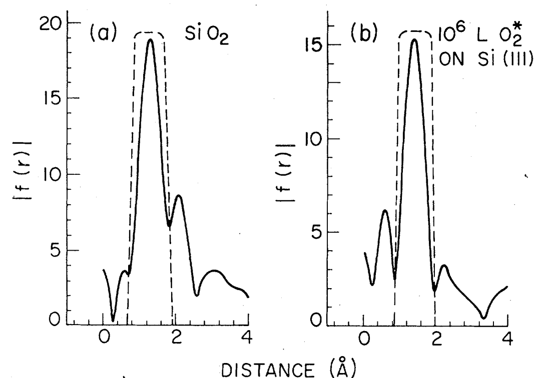

FIG. 15. Absolute value of the Fourier transform $f(r)$ [Eq. (9)] for SiO_2 and oxygen on Si (111) (solid line) and window functions (dashed line) to filter out the O–Si first-neighbor peak.

uncertainty of about equal size to the absolute accuracy of the derived 1.62-Å-neighbor shell separation, we still believe that the small relative *increase* in the O–Si bond length in the oxidized surface complex as compared to SiO_2 is real. Transforming the signal in Fig. 14(a) with the phase shift derived experimentally from the SiO_2 spectrum (assuming a O–Si separation of 1.61 Å in SiO_2) yields a nearest-neighbor distance of 1.65 Å between O and Si atoms on the Si (111) surface. This value should be the more reliable one.

Next, we compare the amplitudes of the SiO_2 and oxygen on Si (111) EXAFS signals by filtering out the nearest-neighbor O–Si peaks in the Fourier transforms $f(r)$ [Eq. (9)] as shown in Fig. 15. The respective amplitudes of the backtransformed signal [Eq. (10b)] are shown in Fig. 16(a). A plot according to Eq. (14) gives almost a straight line with some deviations near the boundaries of the k^2 interval used. We attributed these to termination errors in the Fourier-transformation procedure. The central linear part can be extrapolated to yield a value of 0.66 at $k=0$, corresponding to $N_s^* r_x^2 / N_x^* r_s^2 = 1.94$. Using the values $r_s = 1.61$ Å for SiO_2 and $r_x = 1.65$ Å for oxygen on Si (111) and knowing the coordination number $N_s^* = N_s = 2$ for O in SiO_2, we obtain $N_x^* = 1.1$ for oxygen on Si (111).

From the slope of the curve in Fig. 16, we deduce the relationship $\sigma_s^2 - \sigma_x^2 = 9.25 \times 10^{-3}$ Å^2, meaning that the mean-square relative displacement in SiO_2 is *larger* than for oxygen on Si (111). Unfortunately, the thermal correlation factor σ^2 [Eq. (8)] for thermally grown SiO_2 is not known such that we cannot derive any more detailed quantitative results for σ^2 for the oxygen on the Si (111) system. At first sight, the above result is puzzling because one might expect a larger σ^2 value

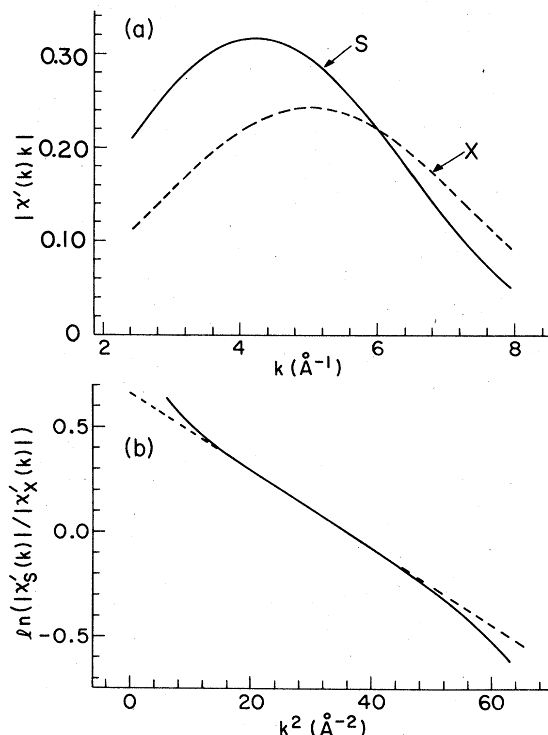

FIG. 16. (a) Absolute value of the backtransformed O–Si nearest-neighbor-peak signal [Eq. (10)] for SiO_2 (curve s) and oxygen on Si (curve x). (b) Natural logarithm of the ratio of curves s and x in (a) as a function of k^2 (solid line). The dashed line extrapolates the linear central part to higher and lower k^2 values. The $k=0$ intercept is 0.66 and the slope is -0.0185 Å^2.

for an O–Si surface complex relative to that in SiO_2. However, it is apparent from Eq. (8) that the EXAFS amplitude is sensitive preferentially to vibrational modes along the bond direction. Thus, an oxygen atom or molecule on the surface could have a sizable vibrational amplitude which does not have a sizable projection along the bond direction and yet a relatively small effective thermal correlation factor σ^2.

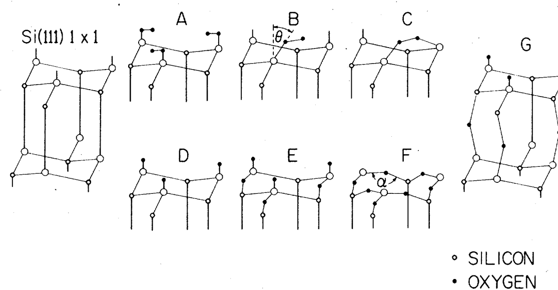

FIG. 17. Model of the unreconstructed Si (111) surface showing the surface and next lower Si double layers and various models for the initial oxidation stages of the (111) surface. The models are compared to experiment in Table II.

In Fig. 17, we show various models for oxygen sorption on Si (111). The structure of the clean unreconstructed Si (111) 1×1 surface is also shown. For simplicity, we neglect the effect of any reconstruction of the Si (111) surface[58] in our further discussion. Most of the models shown in Fig. 17 have been discussed before in conjunction with high resolution electron scattering,[44,59] electron energy loss,[60] photoemission[50,59,61] or Si L-edge partial yield[62] spectra, or theoretical model calculations.[63] We do not show any models which are obviously imcompatible with the derived O–Si bond length of 1.65 Å. The calculated effective coordination numbers for the model geometries in Fig. 17 are listed in Table II. Here, we have used the fact that in our experiments the electric field vector of the incident x rays is almost perpendicular to the surface, i.e., at an angle of 10° from the normal. For this geometry, it is clear from Eq. (7) that, for any O–Si configuration where the bond direction is perpendicular or nearly perpendicular to the surface, a value of N^* significantly larger than 1 will result. For the case of one Si nearest neighbor per O atom, the O–Si bond direction needs to be tilted by $\approx 55°$ from the normal to yield $N^* \approx 1$ as observed experimentally. Thus, models A, D,

TABLE II. Effective coordination numbers calculated for the O–Si surface geometries shown in Fig. 17.

O–Si surface geometry	A	B	C	D	E	F	G
2.9	N_0^* on Si(111)	1.1[a]	1.1	2.9	2.2	1.3–1.5[b]	4.2[c]

[a] Calculated for $\theta \approx 55°$ as in model C.
[b] Corresponding to $90° \lesssim \alpha \lesssim 145°$.
[c] Corresponding to $\alpha = 144°$ as in SiO_2.

E, and G can be excluded. We can also exclude models where oxygen is adsorbed molecularly with the O–O bond direction perpendicular to the surface, e.g., models 3 and 5 in Ref. 44. In this case, an O–O peak of significant intensity should be present in the Fourier transform corresponding to an O–O distance of ~1.2 Å. There is a weak peak in $F(r)$ (Fig. 14) and $f(r)$ (Fig. 15) at lower distance than the main peak A. However, since its intensity is sensitive to the background subtraction procedure used to obtain the EXAFS signal from the original data, we believe it to be at least partially due to the data analysis procedure. Also, its small intensity would only be compatible with a O–O bond direction bent away from the normal.

Models B with $\theta \approx 55°$ and C give a N^* value closest to experiment. The Si–Si distance in the surface plane is 3.84 Å which, with the derived O–Si bond length of 1.65 Å and an assumed O–O bond length of 1.2 Å,[64] yields $\theta = 53°$ for model C. Both models have been proposed before, model B by Rowe *et al.*[59] and model C by Ibach *et al.*[44] Unfortunately, it is not clear whether they investigated the same oxidation stage correponding to a 2.5 eV Si $2p$ core shift since no such measurement was reported. At present, we cannot distinguish between these models. Inspection of the O $1s$ photoemission line should allow a distinction between the two models,[59] but unfortunately in the present experiments the monochromator resolution was insufficient for investigating the expected small splitting for model B. Model F is the only other configuration which is in reasonable agreement with the experimentally derived value for N^*. The calculated values for N^* are found to be relatively insensitive to the Si–O–Si bond angle α (Fig. 17) ranging between 1.3 and 1.5 for $90° \leq \alpha \leq 145°$. At present, we cannot exclude model F. It is interesting to note that *polarization*-dependent surface EXAFS measurements would allow to readily distinguish between models B and C on one side and model F on the other. For example, for x rays incident along the sample normal, one would expect to see a pronounced peak due to the O–O bond in the Fourier transform in case model B or C was correct. Clearly, surface EXAFS measurements in the future should exploit the polarized nature of synchrotron radiation.[20] Polarization-dependent measurements on the same sample also eliminate the problem of possibly different multielectron excitation contributions when comparing the EXAFS amplitudes in different samples as done in the present case. It should then be possible to determine not only bond lengths but also coordination numbers with high accuracy.

VI. CONCLUSIONS

The present paper establishes electron yield EXAFS as a powerful technique for the study of bulk and surface structures. The proposed technique seems to be especially advantageous for experiments in the soft-x-ray region where other detection techniques can only be applied with great experimental difficultly or not at all. Using calculated phase shifts, the determination of bond lengths is possible to an accuracy of less than 0.03 Å which is at least a factor of three better than the capability of low-energy electron diffraction (LEED). With improved data and more reliable phase shifts, it should be possible to determine bond lengths of low-Z atoms in solids and on surfaces to about 0.01 Å, as has previously been demonstrated for intermediate and high-Z atoms.[65] At present, the determination of coordination numbers of atoms or molecules on surfaces by means of surface EXAFS is less reliable than the determination of bond lengths. As shown here, it can be carried out to eliminate certain atomic surface configurations and at least reduce the number of possible models. It is clear, however, from the concepts used and presented here that it should be possible to unambiguously determine surface geometries in many cases by using *polarization*-dependent surface EXAFS. At present, it is already possible to investigate low-Z adsorbate coverages of one monolayer and better signal-to-noise data than presented here for oxygen on Si (111) have already been obtained for oxygen on Ni (100).[13,66] Experimental improvements to obtain spectra for less-than-monolayer coverages are straightforward and include, (i) use of an incident intensity monitor, (ii) improved electron analyzers and detection schemes, and (iii) higher photon flux levels. Many applications of the surface EXAFS technique to different surface crystallographic problems are obvious apart from investigating chemisorption processes on surfaces. These include the study of thin epitaxially grown layers (e.g., Schottky barriers and heterojunctions), the study of small particles on a substrate (e.g., small metal clusters), or the study of clean solid and liquid surfaces in general.

ACKNOWLEDGMENTS

We would like to thank W. E. Spicer for providing the sample chamber and data acquisition system and C. R. Helms for the silicon nitride and oxide samples used in the present study. We have greatly benefitted from discussion with Sally Hunter concerning the EXAFS analysis procedures. The materials incorporated in this work were (partially) developed with the financial support of the NSF under Contract No. DMR 77-27489.

*Permanent address: Hewlett Packard Research Laboratories, 1501 Page Mill Road, Palo Alto, California 94304.

[1]D. E. Sayers, F. W. Lytle, and E. A. Stern, Phys. Rev. Lett. 27, 1204 (1971).

[2]C. B. Duke, J. Vac. Sci. Technol. 15, 157 (1978).

[3]See, for example, A. C. Wright, Adv. Struct. Res. Diffr. Methods 5, 1 (1974).

[4]For a recent review, see, T. E. Fischer, Phys. Today 23 May (1974).

[5]See, for example, I. Lindau, in *International College on Applied Physics*, *Instituto Nazionale di Fisica Nucleare*, edited by A. N. Mancini and I. F. Quercia (Alghero, Italy, 1976); *Electronic Structure and Reactivity of Metal Surfaces*, edited by E. G. Derouane and A. A. Lucas (Plenum, New York, 1976).

[6]J. Stöhr, R. S. Williams, G. Apai, P. S. Wehner, and D. A. Shirley, in *Proceedings of the Fifth International Conference on VUV Radiation Physics*, Montpellier, 1977, edited by M. C. Castex, M. Pouey, and N. Pouey, Vol. II. p. 43.

[7]F. C. Brown, R. Z. Bachrach, S. B. M. Hagström, N. Lien, and C. H. Pruett, in *Vacuum Ultraviolet Radiation Physics*, edited by E. E. Koch, R. Haensel, and C. Kunz (Pergamon, Vieweg, 1974), p. 785; F. C. Brown, R. Z. Bachrach, and N. Lien, Nucl. Instrum. Methods 152, 73 (1978).

[8]J. Stöhr, D. Denley, and P. Perfetti, Phys. Rev. B 18, 4132 (1978).

[9]R. Z. Bachrach (private communication).

[10]For a discussion, see, D. A. Shirley, in Proceedings of the International Workshop on X-ray Instrumentation, SSRL Report No. 78/04 (Stanford University, Stanford, Calif., 1978) (unpublished), p. VII-80.

[11]Wm. J. Veigele, At. Data Tables 5, 51 (1973).

[12]K. Feser, Phys. Rev. Lett. 28, 1013 (1972); H. U. Freund, X-ray Spectrom. 4, 90 (1975).

[13]J. Stöhr, J. Vac. Sci. Technol. 16, 37 (1979).

[14]P. H. Citrin, P. Eisenberger, and B. M. Kincaid, Phys. Rev. Lett. 36, 1346 (1976).

[15]P. A. Lee and G. Beni, Phys. Rev. B 15, 2862 (1977).

[16]Boon-Keng Teo, P. A. Lee, A. L. Simmons, P. Eisenberger, and B. M. Kincaid, J. Am. Chem. Soc. 99, 3854 (1977); P. A. Lee, Boon-Keng Teo, and A. L. Simmons, *ibid*. 99, 3857 (1977). The central atom phase shifts for N and O were supplied by P. A. Lee (private communication).

[17]S. Hunter, Ph.D. dissertation, SSRL Report No. 77/04 (Stanford University, 1977) (unpublished).

[18]J. J. Rehr, E. A. Stern, R. L. Martin, and E. R. Davidson, Phys. Rev. B 17, 560 (1978).

[19]P. H. Citrin, P. Eisenberger, and R. C. Hewitt, Phys. Rev. Lett. 44, 309 (1978).

[20]E. A. Stern, D. E. Sayers, J. G. Dash, H. Shechter, and B. Bunker, Phys. Rev. Lett. 38, 767 (1977); S. M. Heald and E. A. Stern, Phys. Rev. B 17, 4069 (1978).

[21]K. Siegbahn *et al.*, *Electron Spectroscopy for Chemical Analysis*, *Molecular and Solid State Structure by Means of Electron Spectroscopy*, Nova Acta R. Soc. Sci. Ups. Ser. IV 20, 224 (1967).

[22]A. P. Lukirskii and I. A. Brytov, Sov. Phys. Solid State 6, 33 (1964); A. P. Lukirskii and T. M. Zimkina, Izv. Akad. Nauk. SSSR, Ser. Fiz. 28, 765 (1964); A. P. Lukirskii, E. P. Savinov, I. A. Brytov, and Yu. F. Shepelev, Bull. Acad. Sci. USSR Phys. Ser. 28, 774 (1964); A. P. Lukirskii, O. A. Ershov, T. M. Zimkina, and E. P. Savinov, Sov. Phys. Solid State 8, 1422 (1966).

[23]W. Gudat and C. Kunz, Phys. Rev. Lett. 29, 169 (1972).

[24]W. Gudat, Ph.D. thesis (Hamburg University, 1974), Internal Report No. DESY F41-74/10 (unpublished).

[25]G. Martens, P. Rabe, N. Schwentner, and A. Werner, J. Phys. C 11, 3125 (1978).

[26]R. H. Ritchie, F. W. Garber, M. Y. Nakai, and R. D. Birkhoff, Adv. in Radiat. Biol. 3, 1 (1969).

[27]J. L. Stanford, R. N. Hamm, and E. T. Arakawa, J. Opt. Soc. Am. 56, 124 (1966).

[28]I. Lindau and W. E. Spicer, J. Electron Spectrosc. 3, 409 (1974).

[29]S. W. Duckett and P. H. Metzger, Phys. Rev. 137, A953 (1965); A. J. Dekker, *Solid State Physics* (MacMillan, London, 1965).

[30]J. A. R. Samson, *Techniques of Vacuum Ultraviolet Spectroscopy* (Wiley, New York, 1967), p. 34.

[31]G. J. Lapeyre, A. D. Baer, J. Anderson, J. C. Hermanson, J. A. Knapp, and P. L. Gobby, Solid State Commun. 15, 1601 (1974); D. E. Eastman and J. L. Freeouf, Phys. Rev. Lett. 33, 1601 (1974).

[32]R. Z. Bachrach and A. Bianconi, in Ref. 6, Vol. II, p. 213.

[33]P. A. Lee, Phys. Rev. B 13, 5261 (1976); U. Landman and D. L. Adams, Proc. Nat. Acad. Sci. U.S.A. 73, 2550 (1976).

[34]J. Jaklevic, J. A. Kirby, M. P. Klein, A. S. Robertson, G. S. Brown, and P. Eisenberger, Solid State Commun. 23, 679 (1977).

[35]For a tabulation of Auger electron kinetic energies, see: *Handbook of Auger Electron Spectroscopy* (Physical Electronics Industries, Eden Prairie, 1976).

[36]L. A. Harris, Surf. Sci. 15, 77 (1969); W. A. Fraser, J. V. Florio, W. N. Delgass, and W. D. Robertson, *ibid*. 36, 661 (1973); C. S. Fadley, R. J. Baird, W. Siekhaus, T. Novakov, and S. A. L. Bergström, J. Electron Spectrosc. Relat. Phenom. 4, 93 (1974).

[37]G. D. Mahan, Phys. Rev. B 2, 4334 (1970); R. S. Williams, P. S. Wehner, J. Stöhr, and D. A. Shirley, Surf. Sci. 75, 215 (1978).

[38]E. P. Savinov, A. P. Lukirskii, and Yu. F. Shepelev, Sov. Phys. Solid State 6, 2624 (1965).

[39]G. S. Brown, P. Eisenberger, and P. Schmidt, Solid State Commun. 24, 201 (1977).

[40]A. Liebsch, Phys. Rev. Lett. 32, 1203 (1974); A. Liebsch, Phys. Rev. B 15, 544 (1976).

[41]P. A. Lee, Phys. Rev. B 13, 5261 (1976).

[42]For some first experimental results, see, D. A. Shirley, J. Stöhr, P. S. Wehner, R. S. Williams, and G. Apai, Phys. Scr. 16, 398 (1977); S. D. Kevan, D. H. Rosenblatt, D. Denley, B. C. Lu, and D. A. Shirley, Phys. Rev. Lett. 41, 1565 (1978).

[43]P. W. Palmberg, J. Electron Spectrosc. 5, 691 (1974).

[44]H. Ibach, K. Horn, R. Dorn, and H. Lüth, Surf. Sci. 38, 433 (1973).

[45]M. Brown, R. E. Peierls, and E. A. Stern, Phys. Rev. B 15, 738 (1977); S. M. Heald and E. A. Stern, Phys. Rev. B 16, 5549 (1977).

[46]D. Denley, R. S. Williams, P. Perfetti, D. A. Shirley, and J. Stöhr, Phys. Rev. B 19, 1762 (1979).

[47]S. T. Pantelides and W. A. Harrison, Phys. Rev. B 13, 2667 (1976).

[48]O. A. Ershov and A. P. Lukirskii, Sov. Phys. Solid State 8, 1699 (1967).
[49]C. M. Garner, I. Lindau, J. N. Miller, P. Pianetta, and W. E. Spicer, J. Vac. Sci. Technol. 14, 372 (1977).
[50]R. S. Bauer, J. C. McMenamin, H. Petersen, and A. Bianconi, *Proceedings of the International Topical Conference on* SiO_2 *and Its Interfaces*, edited by S. Pantelides (Pergamon, New York, 1978), p. 401.
[51]I. T. McGovern, A. W. Parke, and R. H. Williams, Solid State Commun. 26, 21 (1978).
[52]E. A. Stern, Phys. Rev. B 10, 3027 (1974); C. H. Ashley and S. Doniach, *ibid*. B 11, 1279 (1975); P. A. Lee and J. B. Pendry, *ibid*. B 11, 2795 (1975).
[53]G. Beni and P. M. Platzman, Phys. Rev. B 14, 1514 (1976).
[54]E. A. Stern, D. E. Sayers, and F. W. Lytle, Phys. Rev. B 11, 4836 (1975).
[55]P. Rabe, G. Tolkiehn, and A. Werner, J. Phys. C (to be published); Boon-Keng Teo and P. A. Lee, J. Am. Chem. Soc. (to be published).
[56]G. Martens, P. Rabe, N. Schwentner, and A. Werner, Phys. Rev. B 17, 1418 (1978).
[57]R. W. G. Wyckoff, *Crystal Structures* (Wiley, New York, 1964).
[58]See, for example, D. Haneman, Phys. Rev. 121, 1093 (1961); M. Schlüter, J. R. Chelikowsky, S. G. Louie, and M. L. Cohen, Phys. Rev. B 12, 4200 (1975); W. A. Harrison, Surf. Sci. 55, 1 (1976).
[59]J. E. Rowe, G. Margaritondo, H. Ibach, and H. Froitzheim, Solid State Commun. 20, 277 (1976).
[60]R. Ludeke and A. Koma, Phys. Rev. Lett. 34, 1170 (1975).
[61]C. M. Garner, I. Lindau, C. Y. Su, P. Pianetta, and W. E. Spicer. Phys. Rev. B 19, 3944 (1979).
[62]R. S. Bauer, J. C. McMenamin, R. Z. Bachrach, A. Bianconi, L. Johansson, and H. Petersen, Inst. Phys. Conf. Ser. 43, 797 (1978).
[63]W. A. Goddard III, A. Redondo, and T. C. McGill, Solid State Commun. 18, 981 (1976); W. A. Goddard III, J. J. Barton, A. Redondo, and T. C. McGill, J. Vac. Sci. Technol. 15, 1274 (1978).
[64]For a convenient listing of bond lengths, see, J. C. Slater, *Symmetry and Energy Bands in Crystals* (Dover, New York, 1972), pp. 308–346.
[65]P. Rabe, Jpn. J. Appl. Phys. Suppl. 17-2, 217 (1978).
[66]J. Stöhr, Jpn. J. Appl. Phys. Suppl. 17-2, 22 (1978).